Hydration-drying interactions in a high-volume ground granulated blast-furnace slag mortar

Akli Younsi, Rachid Cherif, Abdelkrim Trabelsi, Ameur Hamami, Rafik Belarbi, Abdelkarim Aït-Mokhtar

Akli Younsi, Rachid Cherif, Abdelkrim Trabelsi, Ameur Hamami, Rafik Belarbi, et al.. Hydration-drying interactions in a high-volume ground granulated blast-furnace slag mortar. Construction and Building Materials, 2021, 279, pp.122427. 10.1016/j.conbuildmat.2021.122427 . hal-03133772

HAL Id: hal-03133772
https://hal.science/hal-03133772v1

Submitted on 13 Feb 2023

Version of Record: https://www.sciencedirect.com/science/article/pii/S0950061821001872
Manuscript_da1e9fe44d784be771da6694b34c20c7

Hydration-Drying interactions in a high-volume ground granulated blast-furnace slag mortar

Akli Younsi [a,*], Rachid Cherif [a], Abdelkrim Trabelsi [b], Ameur El Amine Hamami [a], Rafik Belarbi [a], Abdelkarim Aït-Mokhtar [a]

[a] *La Rochelle University, LaSIE UMR CNRS 7356, Avenue Michel Crépeau, 17042 La Rochelle Cedex 1, France*

[b] *Lyon University, CEL UMR CNRS 5008, INSA-Lyon, Claude Bernard Lyon 1 University, F-69621 Villeurbanne, France*

Authors' e-mail addresses

Akli YOUNSI: akli.younsi@univ-lr.fr

Rachid CHERIF: rachid.cherif@univ-lr.fr

Abdelkrim TRABELSI: abdelkrim.trabelsi@univ-lyon1.fr

Ameur El Amine HAMAMI: ameur_el_amine.hamami@univ-lr.fr

Rafik BELARBI: rafik.belarbi@univ-lr.fr

Abdelkarim AÏT-MOKHTAR: karim.ait-mokhtar@univ-lr.fr

* **Corresponding author:** Akli YOUNSI

Address: La Rochelle University, LaSIE UMR CNRS 7356, Avenue Michel Crépeau, 17042 La Rochelle Cedex 1, France – **Tel.:** +335 46 45 83 85 – **E-mail:** akli.younsi@univ-lr.fr

Abstract

An experimental study of interactions between hydration and early drying was carried out on a mortar with a GGBFS volume as high as the OPC volume. 1 day after casting, the mortar was subjected to 6-month unidirectional drying in natural surrounding conditions in laboratory. At the end of the exposure period, Portlandite content, water porosity and pore size distribution were found to be not uniform along the material. When approaching the exposed surface, due to the early drying, the material gradually becomes less hydrated, more porous, and less dense. This causes strong gradients of transfer properties between the exposed surface and the core of the material, which facilitates exchanges with the surrounding environment near the surface and lowers the resistance against the penetration of aggressive agents. For instance, it was shown that considering properties only within the core of the material, sheltered from drying, significantly underestimates the risk of carbonation, and thus the risk of corrosion of reinforcement in concrete.

Keywords: High-volume GGBFS mortar; Hydration; Early drying; Carbonation; Microstructure; Portlandite content; Water content; $CaCO_3$ content; Water porosity; Pore size distribution

1. Introduction

For environmental considerations, it has become necessary to reduce CO_2 emissions from concrete manufacturing. This is challenged by CO_2 emissions from ordinary Portland cement (OPC) production [1–13], responsible for 65 – 85 % of the CO_2 emissions from concrete manufacturing [9], and for 5 – 8 % of global CO_2 emissions [3,5,10]. About 60 – 70 % of these emissions are generated during production of clinker [1,7,11], which is the main component of OPC. Therefore, efforts to mitigate CO_2 emissions from concrete manufacturing have focused on substituting OPC with industrial by-products, namely supplementary cementitious materials (SCMs) [5,12]. Substituting OPC with ground granulated blast-furnace slag (GGBFS), one of the most common SCMs, offers one of the largest CO_2 mitigation [8,13]. However, the quality of some properties and performances of concrete with high substitution ratio of OPC with GGBFS are lowered compared to OPC concrete [14–20]. In fact, due to the lack of clinker, combined with the slowness of GGBFS reaction, known to be a latent hydraulic SCM, hydration kinetics is strongly slowed down, especially at early age [18–22]. The slowdown of hydration kinetics induces a decrease in hydration level, which reduces the amount of hydrates. This causes an increase in porosity and a coarsening of the microstructure since hydrated phases are known to fill porosity due to their molar volume which is higher than that of anhydrous phases [23–25]. The increase in porosity, combined with the coarsening of the microstructure, induce a coarsening of the properties governing exchanges with the surrounding environment [26,27]. This means an increase, at early age, in sensitivity to transfer of aggressive agents and to hydric transfer [18,28], namely early drying. The latter is known to strongly hamper hydration [23–34], which is already not well advanced because of the high amount of GGBFS. In fact, early drying reduces the amount of water available in the pores, which slows down the hydration kinetics and causes an increase in porosity and a coarsening of the microstructure. The same modifications are induced by shrinkage and modification of some C-S-H phases due to the lack of water evacuated by the early drying [35,36]. Furthermore, early drying induces gradients of properties between the exposed surface and the core of concrete [28,37,38]. The quality of properties within the zone affected by drying should thus be lower than that within the zone sheltered from drying, especially in concrete with high amount of GGBFS, known to be more sensitive to early drying than more conventional concrete [18,28]. A previous theoretical study of interactions between hydration and drying, carried out on concretes with high amount of SCMs, especially GGBFS, showed that, due to drying, hydric, hydration and microstructural properties are not uniform along the material [28]. In fact, when approaching the exposed surface, the material becomes less wet, less hydrated, and more porous. However, characterization of cementitious materials is usually performed within the core sheltered from drying, or even on water-cured specimens, thus well hydrated. For instance, Ballim [39] found that, in the case of concrete with high amount of GGBFS, water-curing at early age had a significant effect on reducing the permeability and water sorptivity of the cover concrete. Sanjuán *et al.* [40] recommended, for concrete with GGBFS, a 7-day water-curing period to guarantee a lower water permeability. The same authors [41] recommended, for mortar with high amount of GGBFS, a 7-day water-curing period to guarantee a lower carbonation rate. Gruyaert *et al.* [42] observed that, for concrete with high amount of GGBFS, an increase in water-curing period from 1 to 3 months increased the resistance against carbonation. However, on construction site, for practical and economic reasons, water-curing is often not applied, which makes early drying unavoidable. Therefore, characterizing water-cured specimens, or within the core sheltered from drying, leads to properties that are often average values along the material. In the case of reinforced concrete, this procedure may overestimate the quality of transfer properties within the cover zone, along which aggressive agents diffuse, and thus may underestimate the risk of corrosion. The latter is probably the most significant cause of degradation in reinforced concrete [43–49]. Initially, reinforcement in concrete is naturally protected against corrosion by the high alkalinity of the pore solution [43]. However, this protection may be hampered by the ingress of chloride ions at a certain threshold (chloride-induced corrosion) [43,44], and/or by the carbonation process which causes the acidification of the pore solution near the steel reinforcement (carbonation-induced corrosion)

[43,48,50]. Despite the importance of the issue, the literature consulted provides few experimental results on effects of interactions between hydration and early drying, especially in the case of cementitious materials with high amount of GGBFS.

In this work, an experimental study of interactions between hydration and early drying was carried out on a high volume GGBFS mortar, namely a mortar designed with a volume of GGBFS as high as the volume of OPC. The objective was to highlight and quantify the effects of early drying on hydration and microstructural properties of the material, especially those governing the carbonation kinetics. For this purpose, the mortar was demolded 1 day after casting and subjected to 6-month unidirectional drying in natural surrounding conditions in laboratory. During the exposure period, the progress of drying front was monitored by continuously recording the relative humidity inside the material, while the drying kinetics was monitored by regular weighing, i.e., by monitoring the mass loss. At the end of the exposure period, hydric profiles were investigated by determining the profile of relative humidity using hygrometric probes, the profile of water content by weighing before and after oven-drying, and the profile of water saturation degree by weighing before and after oven-drying, and after water saturation under vacuum. As natural carbonation occurred during the exposure process, carbonation profile was investigated by determining the profile of $CaCO_3$ by means of a thermogravimetric analysis (TGA), and by phenolphthalein spraying. Hydration profile was investigated by determining the profile of Portlandite content by TGA. A proportionality relationship was assumed between Portlandite content and hydration level. This assumption stems from that of simultaneity of chemical reactions of clinker and GGBFS [51,52]. Finally, microstructural profiles were investigated by determining the profile of porosity by means of water porosity measurement, and the profile of pore size distribution using a mercury intrusion porosimetry (MIP).

2. Experimental procedure

2.1. Raw materials

The study was carried out on a mortar mixture designed with the following constituents: an ordinary Portland cement (OPC) CEM I 52.5 N from Calcia France as per the European Standard EN 197-1 [53], a ground granulated blast-furnace slag (GGBFS) from Ecocem Netherlands as per the European Standard EN 15167-1 [54], and a siliceous sand (0/4 mm) from HeidelbergCement France as per the European Standard EN 13139 [55]. The sand, which has a density of 2600 kg/m^3, does not contain $CaCO_3$, while about 8.7 and 1.0 % of $CaCO_3$ were measured by TGA in OPC and GGBFS, respectively. OPC was stored under hermetically sealed conditions before use to limit its exposition to the atmospheric humidity and CO_2. Despite these precautions, a slight natural carbonation occurred on the cement surface, which formed the CaO_3 measured. Table 1 shows the properties of the cementitious materials used.

Table 1

Physical, mineralogical, and chemical properties of OPC and GGBFS, supplied by the manufacturers.

	OPC	GGBFS
Physical properties		
Density [kg/m^3]	3180	2890
Blaine surface [cm^2/g]	4050	4500
Composition [%]		
Clinker	95.1	-
Gypsum	4.9	-
Clinker mineralogical composition [%]		
C_3S	67	-
C_2S	13	-
C_3A	7	-
C_4AF	13	-
Chemical composition [%]		
CaO	64.2	41.5
SiO_2	20.5	33.3
Al_2O_3	5.0	12.5
Fe_2O_3	3.9	0.4
SO_3	2.5	0.2
MgO	1.1	7.0

2.2. Mix-design procedure

The proportions used in the mix are given in Table 2. The mortar mixture was prepared using the mix-design method described by Eqs. 1 to 4:

$$V_S + V_C + V_A + V_W = 1\ \mathrm{m}^3 \tag{1}$$

$$V_C + V_A + V_W = 0.459\ \mathrm{m}^3 \tag{2}$$

$$\frac{W}{A + C} = 0.535 \tag{3}$$

$$\frac{A}{A + C} = 0.482 \tag{4}$$

with: V_S, V_C, V_A and V_W [m^3] are the sand, OPC, GGBFS and water volumes, respectively. W, A and C [kg] are the effective water, GGBFS and OPC contents per cubic meter of mortar, respectively. The volume of sand (V_S) was fixed equal to 0.542 m^3 to obtain a paste volume of 0.459 m^3 (Eq. 2) [56]. The water-to-binder ratio was taken equal to 0.535 (Eq. 3). Such values of paste volume and water-to-binder ratio were chosen to obtain a homogeneous mortar mixture, by limiting bleeding and segregation, and to ensure its good workability [56]. Moreover, the water-to-binder ratio was chosen enough high to mitigate the phenomenon of self-desiccation due to hydration [29,57]. The cement substitution ratio was fixed equal to 0.482 (Eq. 4) to maintain the GGBFS volume (V_A) as high as the OPC volume (V_C). The cement substitution ratio deliberately exceeded the maximum value of 0.3 allowed by the specifications of the European Standard EN 206+A1 [58] which accounts for durability when designing concrete. The mortar obtained can thus be qualified as a high-volume GGBFS mortar according to the normative framework. It should be noted that a higher substitution ratio lowers the quality of some properties and performances of the material due to the lack of clinker [14–20]. The study was carried out on mortar specimens instead of concrete specimens to shorten the exposure period (Section 2.4). The mortar specimens were chosen enough representative (Section 2.3) to extend the obtained findings to concrete with the same GGBFS content.

Table 2

Mix proportions per cubic meter of mortar.

	Content [kg]	Volume [l]
Sand 0/4	1409	542
CEM I 52.5 N	275	86
GGBFS	256	88

Effective water	284	284

2.3. Mortar mixture casting

The mortar mixture was cast, according to the European Standard EN 196-1 [59], into eight 75X75X75 mm molds and stored in a room at 20 ± 1 °C for 24 h. Such a mold size corresponds to the maximum stroke of the saw used to cut the different specimens according to the needs and purposes of each test. The eight 75X75X75 mm specimens were demolded 1 day after casting to submit the mortar to an early drying.

2.4. Exposure procedure

Immediately after demolding at 1 day, the faces of the eight 75X75X75 mm specimens, including the top and the bottom, were covered by an adhesive aluminum, except for one lateral face, to ensure unidirectional exchanges with the surrounding environment [19]. After that, all the 75X75X75 mm specimens were subjected to drying and natural carbonation for 6 months. The exposure was carried out in a room where the temperature and the relative humidity were continuously monitored by a sensor. The temperature (T_e) ranged between 18 and 27 °C and the relative humidity (RH_e) between 64 and 70 % (Fig. 2). Punctual measurements of the ambient CO_2 concentration showed that it ranged between 380 and 460 ppm. Among the eight 75X75X75 mm specimens, 6 specimens were regularly weighed to monitor the drying kinetics during the 6-month exposure period. The other two 75X75X75 mm specimens were used to determine the profile of relative humidity inside the specimens, and to monitor the progress of drying front.

2.5. Profiles determination after 6-month exposure

Hydric, carbonation, hydration and microstructural profiles were determined on eight 75X75X75 mm specimens after 6 months of exposure following the protocols described in the following sections.

2.5.1. Hydric profiles

The hydric profiles were investigated by determining the profiles of relative humidity, water content and water saturation degree.

- The profile of relative humidity was determined on two 75X75X75 mm specimens, with five sides covered by an adhesive aluminum, using hygrometric probes placed inside four Ø10X40 mm holes. The probes had an accuracy of ± 2 % from 0 to 90 % relative humidity, and ± 4 % from 90 to 100 % relative humidity. The holes were drilled in each specimen immediately after demolding at 1 day [19]. The centers of the holes were located at different distances: 10, 28, 47 and 65 mm from the exposed surface, as indicated in Fig. 1-a. The tops of the holes were sealed by a silicone sealant and covered by an adhesive aluminum. The relative humidity inside the specimens was continuously recorded for 6 months to monitor the progress of drying front within the material.
- The profiles of water content and water saturation degree were determined on twelve 10X75X75 mm samples saw-cut from two 75X75X75 mm specimens perpendicularly to the exchanges direction, as indicated in Fig. 1-b. Immediately after sawing in dry conditions, using a 3 mm saw blade, the 10X75X75 mm samples were weighed. Then, they were oven-dried at 55 ± 5 °C until the equilibrium characterized by an insignificant relative mass variation, corresponding to a relative mass loss within 24 h less than

0.005 % [60,61]. After that, the 10X75X75 mm samples were water-saturated under vacuum according to the French Standard NF P18-459 [62]. The procedure consists of placing samples inside a desiccator where the pressure is maintained below 25 mbar for at least 4 ± 0.5 h. The water saturation is then performed such that the samples are totally immersed after 15 min. The reduced pressure is maintained for 44 ± 1 h.

2.5.2. Carbonation profile

The carbonation profile was studied by determining the profile of $CaCO_3$. Measurements were carried out by a thermogravimetric analysis (TGA) [18,19,34,56,63] performed on 14 powder samples of 230 ± 15 mg. The powders were obtained by drilling [19] Ø6X75 mm holes in two 75X75X75 mm specimens at different distances: 7, 13, 23, 36, 53, and 68 mm from the exposed surface, as indicated in Fig. 1-c. The powders were tested, immediately after drilling to avoid their carbonation, using a Setaram Setsys Evolution® device with a heating rate of 10 °C/min from 20 to 1000 °C in an Argon atmosphere [18,19,34,56,63]. Moreover, the two 75X75X75 mm specimens were split in half, and a *pH* indicator solution, namely phenolphthalein, was sprayed on the split sections to assess the carbonation depth according to the European Standard EN 12390-12 [64].

2.5.3. Hydration profile

The hydration profile was investigated by determining the profile of Portlandite. Measurements were carried out by TGA [18,19,34,56,63], at the same time, and on the same powder samples as the determination of the $CaCO_3$ profile (Fig. 1-c).

2.5.4. Microstructural profiles

The microstructural profiles were investigated by determining the profiles of porosity and pore size distribution.

- The profile of porosity was studied by determining the profile of water porosity. Measurements were carried out, according to the French Standard NF P18-459 [62], at the same time, and on the same 10X75X75 mm samples as the determination of the water content and water saturation degree profiles (Fig. 1-b).
- The profile of pore size distribution was determined by mercury intrusion porosimetry (MIP), which was carried out on ten 10 mm cubic samples saw-cut from the cores of ten 10X75X75 mm samples, themselves saw-cut from two 75X75X75 mm specimens perpendicularly to the exchanges direction, as shown in Fig. 1-d. Measurements were performed according to the International Standard ISO 15901-1 [65]. A Micromeritics Autopore V 9620® porosimeter was used with a pressure larger than 400 MPa. This allowed pore diameter determination in the range from 0.003 µm to 360 µm.

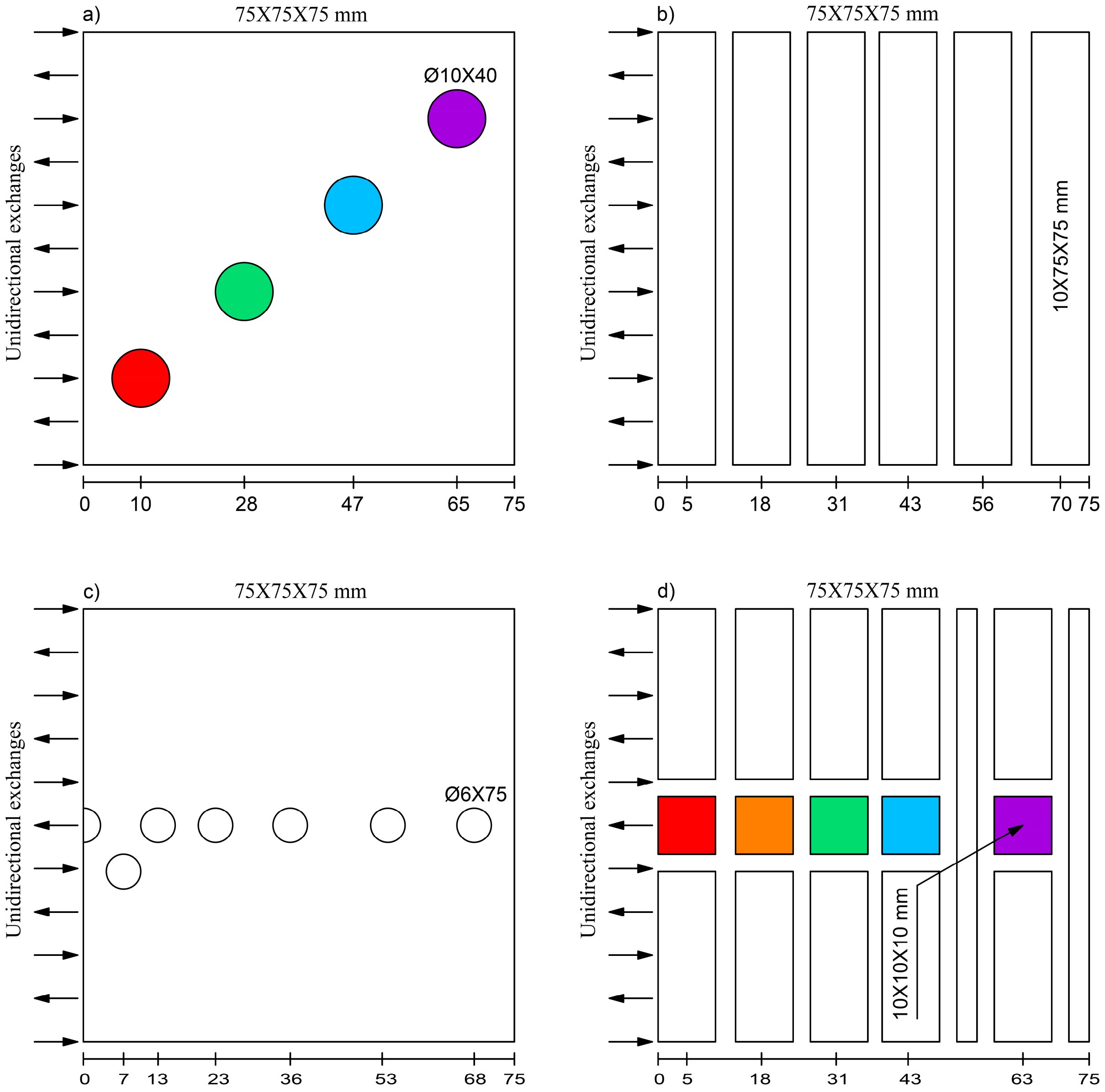

Fig. 1. Top views of the specimens used to determine the profiles of: **(a)** relative humidity, **(b)** water content, water saturation degree and water porosity, **(c)** $CaCO_3$ and Portlandite contents by TGA, and **(d)** pore size distribution by MIP.

3. Results and discussion

3.1. Drying kinetics

3.1.1. Drying front

The progress of drying front was monitored for 6 months by continuously recording the relative humidity inside two 75X75X75 mm specimens. Fig. 2 shows the time-evolution of the relative humidity measured by probes at different locations inside the material. At the beginning of the exposure process, all the probes indicate 100 % relative humidity. After that, the probes placed at 10, 28 and 47 ± 5 mm indicate a relative humidity drop after about 0.23, 2 and 5 months of exposure, respectively. A slight decrease in relative humidity due to self-desiccation should appear all along the material [66]. The phenomenon of self-desiccation is defined as the decrease in relative humidity inside the pores which occurs when the amount of water strongly decreases due to its consumption by hydration [29,57,66]. However, due to their accuracy of ± 4 %, the probes placed at 65 ± 5 mm indicate 100 % relative humidity even after 6-month exposure. The water-to-binder ratio used (Eq. 3) is thus enough to mitigate the phenomenon of self-desiccation. This means that, without drying, the amount of water not yet consumed by hydration, and remaining in the pores, is enough to maintain the relative humidity at least at 96 %, given the probes accuracy. Therefore, the beginning of the decrease in relative humidity, i.e., its drop below 100 %, which appears after a short equilibrium period corresponding to the response time of the probes, is attributed to the drying. As mentioned above, Fig. 2 shows that the drying front reaches 10, 28 and 47 ± 5 mm after about 0.23, 2 and 5 months of exposure, respectively, i.e., with the average velocities of 1.39 ± 0.71, 0.47 ± 0.08 and 0.31 ± 0.03 mm/day, respectively. The evolution of these velocities indicates that the drying front progresses quickly within the first few millimeters from the exposed surface. This occurs during the first week of exposure, corresponding to 0.23 months. After that, the progress of the drying front gradually slows down without reaching 65 ± 5 mm at the end of the exposure period.

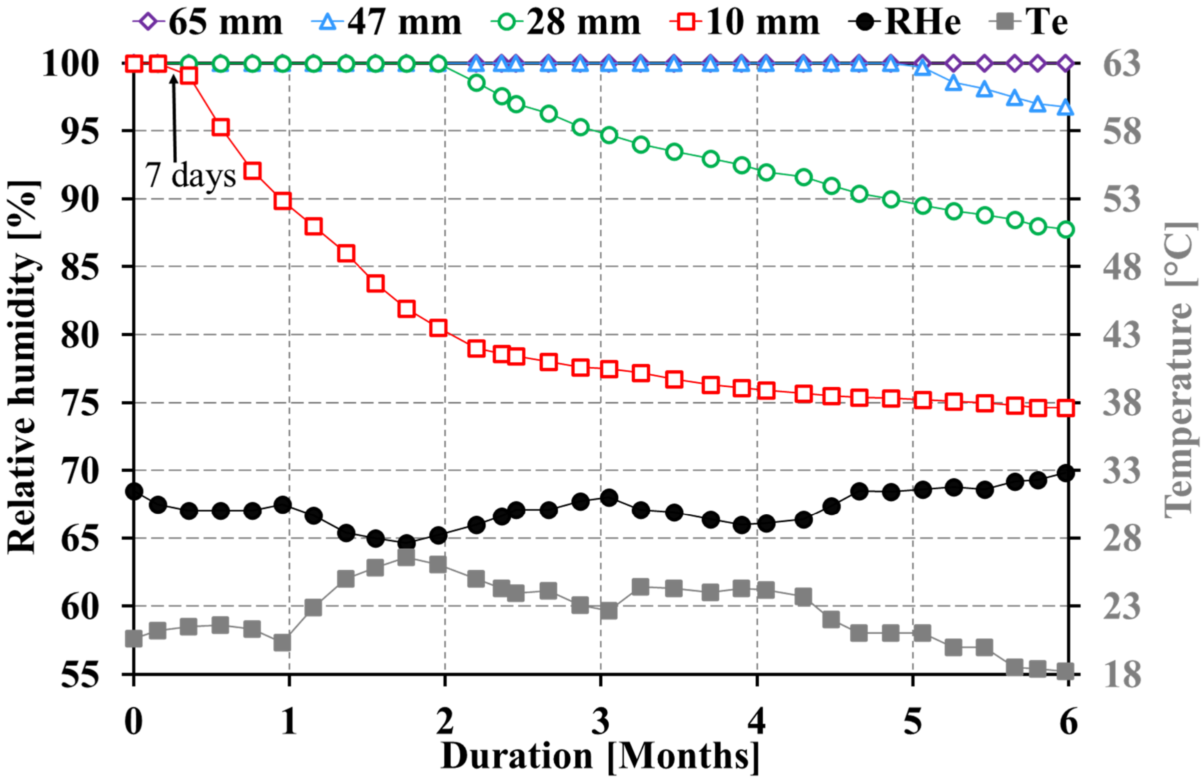

Fig. 2. Time-evolutions of the relative humidity at different locations inside the material, external relative humidity (RH_e) and external temperature (T_e) monitored during the 6-month exposure period.

3.1.2. Water loss

The drying kinetics was monitored for 6 months by regularly weighing six 75X75X75 mm specimens. Fig. 3 shows the time-evolution of the relative water loss calculated by Eq. 5:

$$\Delta w/w_0 = \Delta m/m_0 \frac{S+C+A+W}{W} = \frac{m-m_0}{m_0}\frac{S+C+A+W}{W}100 \tag{5}$$

with: $\Delta w/w_0$ and $\Delta m/m_0$ [%] are the relative water loss and material relative mass loss at a given time, respectively. S, C, A and W [kg] are the sand, OPC, GGBFS and effective water contents per cubic meter of mortar, respectively. m and m_0 [kg] are the material mass at a given time and material initial mass measured at the beginning of the exposure process, respectively. Fig. 3 shows that the drying kinetics is fast at early age. The relative water loss calculated at the end of the first week of exposure is about – 6.29 %, corresponding to a water loss of about – 17.86 kg per cubic meter of mortar. This represents 59 % of the relative water loss of – 10.66 % reached at the end of the exposure period. Beyond a week of exposure, the drying kinetics gradually slows down and tends towards the equilibrium after 5 months of exposure, without reaching a full equilibrium at the end of the exposure period. The behavior of the drying kinetics, expressed by the water loss (Fig. 3), is consistent with that of the drying front progress (Fig. 2). The fast drying which occurs along the first few millimeters from the exposed surface, during the first week of exposure, is followed by a gradual slowdown. This behavior can be explained by the combination of several factors:

At early age, hydration of the binder, composed of OPC and GGBFS, is not well advanced because of the high amount of GGBFS, known to be a latent hydraulic SCM [14–22]. This results in a material which contains a large amount of water not yet reacted, especially since a relatively high water-to-binder ratio is used. The unreacted water is evacuated towards the surface layer of the exposed surface, in liquid form, by the capillary pressure which predominates the hydric transport at the beginning of the exposure process. In this case, only the advection of the liquid phase is considered since the pores are close to saturation. The evacuated water finally evaporates at the surface layer of the exposed surface. Moreover, along the first few millimeters from the exposed surface, low hydration level, combined with early drying which hampers hydration [23–34], lead to a material with a high porosity and coarse microstructure and transfer properties. This facilitates the water evacuation and its evaporation, and thus accelerates the kinetics of drying.

Beyond a week of exposure, the amount of water gradually decreases due to its consumption by hydration and drying. Furthermore, the water evacuation towards the surface layer of the exposed surface can still occur in liquid form when the liquid phase remains continuous, and in gaseous form since the pores are not saturated. Two modes of hydric transport can thus be considered: the advection of the continuous liquid phase, where the evacuated water evaporates at the surface layer of the exposed surface, and the diffusion of the gaseous phase towards the surface layer of the exposed surface, where the evaporation occurs beforehand inside the pores. Interactions between liquid and gaseous phases [67], corresponding to evaporation-condensation interactions in the pores, contribute to gradually slowing the kinetics of drying. Finally, hydration products, namely hydrates, combined with the main carbonation product, namely $CaCO_3$ which is formed within the first few millimeters from the exposed surface (Fig. 6), gradually reduce the porosity and lead to denser microstructure and transfer properties, and thus slow down the kinetics of drying.

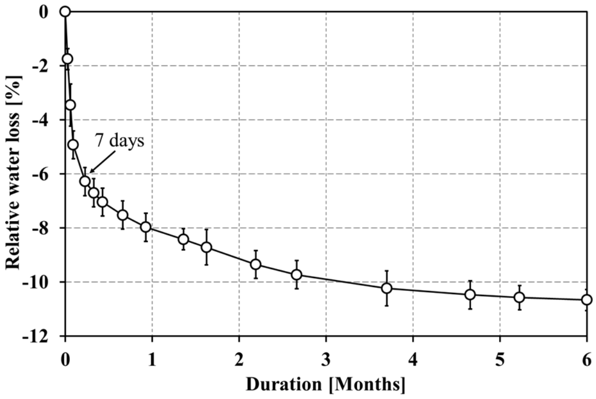

Fig. 3. Time-evolution of the relative water loss monitored during the 6-month exposure period.

3.2. Profiles after 6-month exposure

The following sections report the results obtained after 6-month exposure. It should be noted that the skin-effect [68] due to the contact with the mold was neglected in the discussion since it only occurs within the first few millimeters from the exposed surface.

3.2.1. Drying depth

Fig. 4 shows a schematic presentation of the profiles of relative humidity (RH), water content (U), water saturation degree (S), Portlandite content (CH) and water porosity (ε) obtained after 6-month exposure. The profiles show that the properties studied are not uniform all along the material. There is a strong gradient between the exposed surface and the core of the material sheltered from drying. As explained in the following sections, the beginning of the decrease in RH, U, S and CH, and increase in ε, is attributed to the drying. The distance between the exposed surface and the drying front is called "drying depth". It corresponds to the depth along which the shape of each profile is strongly affected by drying.

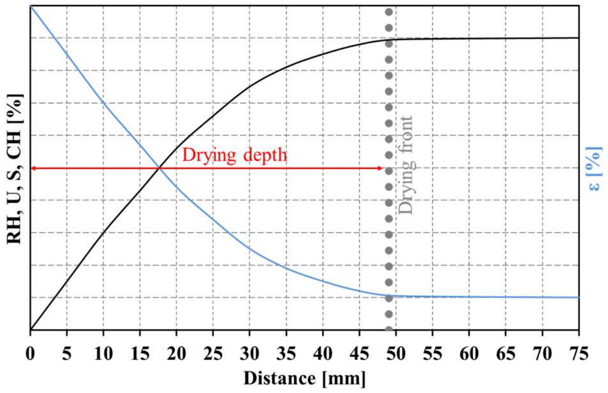

Fig. 4. Schematic presentation of the profiles of relative humidity (RH), water content (U), water saturation degree (S), Portlandite content (CH) and water porosity (ε) obtained after 6-month exposure.

3.2.2. Hydric profiles

To monitor the progress of drying front, relative humidity was continuously recorded inside two 75X75X75 mm specimens using probes placed at different distances from the exposed surface. The results obtained at the end of the 6-month exposure period allowed plotting the profile of relative humidity shown in Fig. 5-a. The profiles of water content and water saturation degree after 6-month exposure were determined on twelve 10X75X75 mm samples saw-cut from two 75X75X75 mm specimens perpendicularly to the exchanges direction (Fig. 5-b). The water content and water saturation degree were calculated by Eqs. 6 and 7, respectively:

$$U = \frac{m_{wet} - m_{dry}}{m_{dry}} 100 \tag{6}$$

$$S = \frac{U}{U_{sat.}} 100 = \frac{m_{wet} - m_{dry}}{m_{sat.} - m_{dry}} 100 \qquad (7)$$

with: U [%] is the water content. m_{wet} and m_{dry} [kg] are the material masses measured at the end of the exposure period and after oven-drying at 55 ± 5 °C, respectively. S [%] is the water saturation degree. $U_{sat.}$ [%] is the saturated water content. $m_{sat.}$ [kg] is the material mass after water-saturation under vacuum. Fig. 5 shows that the relative humidity, water content and water saturation degree are not uniform all along the material. This proves the slowness of achieving a hydric balance between the entire pore network of the material and the surrounding environment. Based on the results of drying front (Section 3.1.1), the beginning of the decrease in relative humidity, water content and water saturation degree is attributed to the drying. According to the relative humidity curve, and given the positions and diameters of the probes, the location of the drying front is approximately assessed between 42 and 60 mm (Fig. 5-a), while, according to the water content and water saturation degree curves, the location of the drying front is approximately assessed between 38 and 51 mm (Fig. 5-b). Finally, in terms of hydric profiles, the location of the drying front can be affined to about 49 mm, which corresponds to the depth along which the shape of the profiles is strongly affected by drying (Fig. 4).

Along the drying depth, the gradual decrease in relative humidity, compared to the initial 100 % relative humidity, in water content, compared to the initial water content calculated from the composition (Table 2), i.e., W/(S+C+A) = 14.64 %, and in water saturation degree, compared to the full saturation, i.e., S = 100 %, is due to the gradual decrease in the amount of water in the pores, itself due to the gradual increase in water consumption by hydration and drying. As shown in Fig. 7, the Portlandite content, expressing the hydration level, decreases when approaching the exposed surface, mainly due to the retarding effect of drying on hydration. This implies that the amount of water consumed by hydration decreases when approaching the exposed surface. It is thus possible to conclude that the shape of the hydric profiles is essentially due to the water consumption by drying which increases when approaching the exposed surface. Furthermore, the relative humidity, water content and water saturation degree strongly decrease when approaching the exposed surface to establish a balance between the entire pore network and the surface layer. For instance, compared to the initial 100 % relative humidity, the decrease in relative humidity measured at 10 ± 5 mm is about – 25 %. Compared to the initial water content calculated from the composition, the decrease in water content measured at 5 ± 5 mm represents a relative water content loss of about – 82.23 %. Compared to the full saturation, the decrease in water saturation measured at 5 ± 5 mm is about – 72.05 %.

Beyond the drying front, the assumed slight decrease in relative humidity (undetected by the probes, as explained in Section 3.1.1), compared to the initial 100 % relative humidity, the decrease in water content, compared to the initial water content calculated from the composition, and the decrease in water saturation degree, compared to the full saturation, are only due to water consumption by hydration. The decrease in water content corresponds to a relative water content loss of about – 44.81 %. This represents a water loss of about – 117.74 kg per cubic meter of mortar. The latter is calculated by considering that the decrease in water content does not generate any material mass loss. In fact, as the core of the material is sheltered from drying, water is just transformed by reacting to produce hydrates. The decrease in water saturation degree is about – 8.07 %. The water content and water saturation degree measured are thus generated by the unreacted water remaining in the pores after 6-month hydration. Furthermore, as the core of the material is sheltered from drying, it contains the highest amount of water available in the pores. This leads to the highest relative humidity, the highest water content, and the highest water saturation degree.

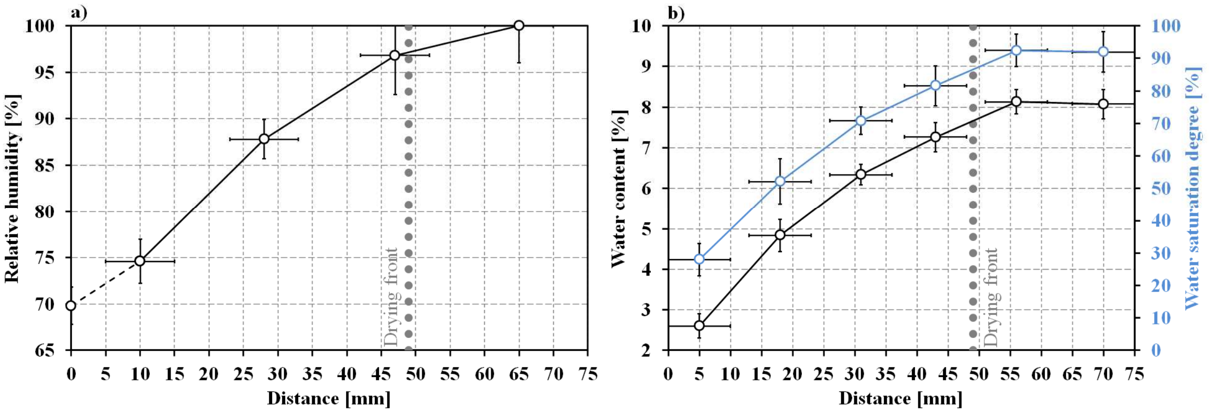

Fig. 5. Profiles of: **(a)** relative humidity, **(b)** water content and water saturation degree obtained after 6-month exposure.

3.2.3. Carbonation profile

The profile of carbonation after 6-month exposure was studied by determining the profile of $CaCO_3$ (Fig. 6). Measurements were carried out by TGA performed on 14 powder samples of 230 ± 15 mg. The $CaCO_3$ content was calculated by Eq. 8:

$$\mathrm{CaCO_3} = \frac{\Delta m_{T_{C1}\rightarrow T_{C2}}}{m_p}\,\frac{M_{CaCO_3}}{M_{CO_2}}\,100 \tag{8}$$

with: $CaCO_3$ [%] is the $CaCO_3$ content. $\Delta m_{T_{C1}\rightarrow T_{C2}}$ [kg] is the powder mass loss between the tangents of the thermogravimetry curve at two temperatures: $T_{C_1} \approx 540$ °C and $T_{C_2} \approx 850$ °C determined more accurately with the derivative thermogravimetry DTG. m_p [kg] is the powder mass. M_{CaCO_3} and M_{CO_2} [kg/mol] are the molecular weights of $CaCO_3$ and CO_2, respectively. Fig. 6 shows that the $CaCO_3$ content is uniform along the material, except for the first few millimeters from the exposed surface affected by carbonation. In fact, a carbonation depth of about 5 ± 1 mm is assessed using phenolphthalein sprayed on the split sections of the two 75X75X75 mm specimens used to carry out the TGA analysis. The assessed carbonation depth is lower than the assessed drying depth of about 49 mm. This proves that the kinetics of drying is faster than the kinetics of naturel carbonation. The latter is mainly controlled by two phenomena: diffusion of CO_2 gas into the pores, and chemical reactions between the dissolved CO_2 and the carbonatable products of the cement-based matrix, as explained in section 3.2.6.

Within the carbonated zone, the $CaCO_3$ content measured at 7 ± 3 mm and at the material surface layer is about 4 times and about 8 times higher than that measured within the core of the material, respectively. This confirms the carbonation depth of about 5 ± 1 mm assessed by phenolphthalein. Furthermore, the $CaCO_3$ content strongly increases when approaching the exposed surface where the conditions required for carbonation are optimal in terms of CO_2 availability, hydric conditions, and amount of carbonatable products, as detailed in section 3.2.6. Finally, as mentioned in section 3.1.2, the carbonation within the first few millimeters from the exposed surface contributes, through the precipitation of the main carbonation product, namely $CaCO_3$, to the reduction of porosity, and to the densification of microstructure and transfer properties, and thus to the slowdown of kinetics of drying.

Along the non-carbonated zone, there is about 1.09 ± 0.14 % of $CaCO_3$ despite the absence of carbonation. As mentioned in section 2.1, the sand does not contain $CaCO_3$, while there is about 8.7 and 1.0 % of $CaCO_3$ in OPC and GGBFS, respectively. Given the composition of 1 m^3 of mortar (Table 2), this corresponds to about 1.07 % of $CaCO_3$ supplied by OPC, and about 0.11 % supplied by GGBFS. The non-carbonated material thus contains about 1.18 % of $CaCO_3$, which is close to the value of 1.09 ± 0.14 % assessed by TGA.

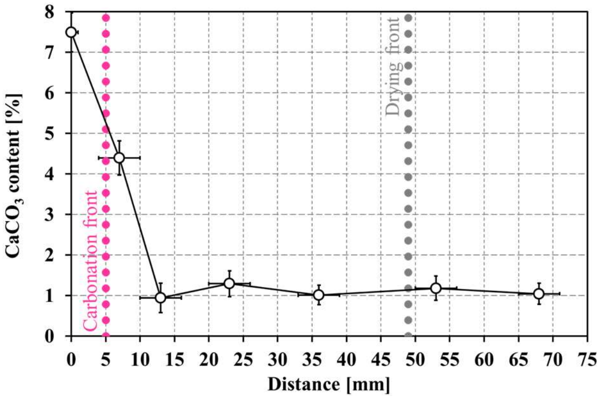

Fig. 6. Profile of $CaCO_3$ content obtained after 6-month exposure.

3.2.4. Hydration profile

The profile of hydration after 6-month exposure was investigated by determining the profile of Portlandite content by a thermogravimetric analysis (TGA) performed on 14 powder samples of 230 ± 15 mg (Fig. 7). A proportionality relationship is assumed between the Portlandite content and the hydration level. This assumption stems from that of simultaneity of chemical reactions of clinker and GGBFS [51,52]. The Portlandite content was calculated by Eq. 9:

$$\mathrm{CH} = \frac{\Delta \mathrm{m}_{\mathrm{T_{P1}} \rightarrow \mathrm{T_{P2}}}}{\mathrm{m_p}} \frac{\mathrm{M_{CH}}}{\mathrm{M_{H_2O}}} 100 \tag{9}$$

with: CH [%] is the Portlandite content. $\Delta \mathrm{m}_{\mathrm{T_{P1}} \rightarrow \mathrm{T_{P2}}}$ [kg] is the powder mass loss between the tangents of the thermogravimetry curve at two temperatures: $\mathrm{T_{P_1}} \approx 410$ °C and $\mathrm{T_{P_2}} \approx 580$ °C determined more accurately with the derivative thermogravimetry DTG. $\mathrm{m_p}$ [kg] is the powder mass. $\mathrm{M_{CH}}$ and $\mathrm{M_{H_2O}}$ [kg/mol] are the molecular weights of Portlandite and water, respectively. Fig. 7 shows that the Portlandite content is not uniform along the material. As for the hydric profiles (Fig. 5), the curve of Portlandite content exhibits a drying depth of about 49 mm along which the shape of the profile is strongly affected by drying (Fig. 4).

Along the drying depth, the shape of the Portlandite content profile follows that of the hydric profiles (Fig. 5). The gradual decrease in Portlandite content, compared to the value within the core of the material, is due to the gradual decrease in water content. For instance, the beginning of the decrease in Portlandite content (Fig. 7), occurring at about 49 mm, corresponds to a relative humidity of about 97 ± 4 % (Fig. 5-a). This is consistent with the literature which shows that hydration, thus the formation of Portlandite, is hampered even at a high relative humidity [23–34]. Furthermore, the Portlandite content strongly decreases when approaching the exposed surface. Compared to the value within the core of the material, the decrease in Portlandite content measured at 7 ± 3 mm represents a relative Portlandite content loss of about – 41.43 %. At the material surface layer, TGA measurements do not detect any Portlandite. This can be explained by the combination of three parameters: (a) Hydration of GGBFS, which is a latent hydraulic SCM that does not produce Portlandite, is known to consume a part of the Portlandite supplied by clinker, itself supplied by OPC used, to produce other hydrates. During 6-month hydration, there is thus a competition between the production of Portlandite by clinker and its consumption by GGBFS. (b) Early drying, occurring at the material surface layer, strongly slows down the hydration kinetics, and thus the production of Portlandite, which is already not well advanced because of the high amount of GGBFS. (c) Carbonation, occurring within the first few millimeters from the exposed surface (Fig. 6), consumes a part of the Portlandite produced.

Beyond the drying front, the amount of Portlandite corresponds to that remaining from the 6 months of competition between its production by clinker and its consumption by GGBFS. Furthermore, as the core of the material is sheltered from drying, it contains the highest amount of water available in the pores, which leads to the highest hydration level, and thus to the highest Portlandite content.

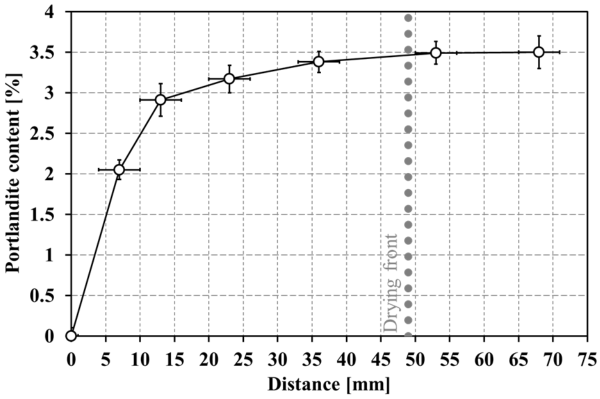

Fig. 7. Profile of Portlandite content obtained after 6-month exposure.

3.2.5. Microstructural profiles

- ***Porosity***

The profile of porosity after 6-month exposure was studied by determining the profile of water porosity (Fig. 8-a). Measurements were carried out on twelve 10X75X75 mm samples saw-cut from two 75X75X75 mm specimens perpendicularly to the exchanges direction. The water porosity was calculated by Eq. 10:

$$\varepsilon = \frac{m_{sat.} - m_{dry}}{\rho_w\, V_s}\, 100 \tag{10}$$

with: ε [%] is the water porosity. $m_{sat.}$ and m_{dry} [kg] are the material masses measured after water-saturation under vacuum and after oven-drying at 55 ± 5 °C, respectively. ρ_w [kg/m^3] is the water density. V_s [m^3] is the material volume measured by hydrostatic weighing. Fig. 8-a shows that the water porosity is not uniform all along the material. As for the hydric and hydration profiles (Figs. 5 and 7), the curve of water porosity exhibits a drying depth of about 49 mm along which the shape of the profile is strongly affected by drying (Fig. 4).

Along the drying depth, the shape of the water porosity profile is opposite to that of the hydric and hydration profiles (Figs. 5 and 7). The gradual increase in water porosity, compared to the value within the core of the material, is due to the gradual decrease in hydration level, expressed by the Portlandite content (Fig. 7), itself due to the gradual decrease in the amount of water available in the pores, as discussed in section 3.2.4. The decrease in hydration level, due to drying, reduces the amount of hydrates, and thus increases the porosity since hydrated phases are known to fill porosity due to their molar volume which is higher than that of anhydrous phases [23–25]. Drying also induces a shrinkage and a modification of some C-S-H phases due to water evacuation and evaporation [35,36]. These modifications, which cause a coarsening of the microstructure (Fig. 8-b), increase the porosity. The water porosity strongly increases when approaching the exposed surface. Compared to the value within the core of the material, the water porosity measured at 5 ± 5 mm represents a relative water porosity gain of about + 8.03 %. Furthermore, the water porosity at 5 ± 5 mm slightly decreases compared to the value at 18 ± 5 mm due to the partial carbonation occurring within the first few millimeters from the exposed surface (Fig. 6), i.e., within half of the thickness of the 10X75X75 mm samples tested (Fig. 1-b). In fact, carbonation is known to reduce porosity through the precipitation of the main carbonation product, namely $CaCO_3$.

Beyond the drying front, as the core of the material is sheltered from drying, it contains the highest amount of water available in the pores. This leads to the highest hydration level, which leads to the highest amount of hydrates, and thus to the lowest porosity.

- ***Pore size distribution***

The profile of pore size distribution after 6-month exposure was determined by a mercury intrusion porosimetry (MIP) carried out on ten 10 mm cubic samples saw-cut from the cores of ten 10X75X75 mm samples, themselves saw-cut from two 75X75X75 mm specimens perpendicularly to the exchanges direction (Fig. 8-b). The previous sections show that in terms of hydric, hydration and porosity results (Figs. 5, 7 and 8-a), drying front is located at about 49 mm. The curve of pore size distribution measured at 63 ± 5 mm is thus located within the core of the material sheltered from drying, while the other curves are located within the zone affected by drying (Fig. 8-b).

Within the zone affected by drying, compared to the curve determined at 63 ± 5 mm, the curves exhibit a gradual coarsening of the gel porosity, with a gradual decrease in the amount of gel pores when approaching the exposed surface. The gel pores are defined as pores with widths between 0.002 and 0.008 μm [69]. The curves also exhibit a gradual coarsening of the capillary porosity, with a gradual shift of the critical diameter peak towards the large pore diameters when approaching the exposed surface. The capillary pores are defined as pores with widths between 0.008 and 10 μm [69]. Drying thus causes a gradual coarsening of the microstructure when approaching the exposed surface. This can be explained by the combination of two parameters: (a) Drying reduces the amount of water available in the pores, which reduces the hydration level, and thus reduces the amount of hydrates, known to fill porosity. The lack of hydrates causes a coarsening of the microstructure. (b) Drying causes a shrinkage and a modification of some C-S-H phases due to water evacuation and evaporation [35,36]. This decreases the amount of gel pores and increases the amount of capillary pores, without any effect on the drying kinetics. Such modifications of porosity induce the coarsening of the microstructure. Furthermore, compared to the curve obtained at 18 ± 5 mm, the curve measured at 5 ± 5 mm exhibits a densification of the capillary porosity, which is accompanied by a slight decrease in porosity (Fig. 8-a). This is due to the partial carbonation, mentioned previously, which fills the capillary porosity by precipitation of $CaCO_3$. The curve also exhibits an increase in the amount of capillary pores, with widths between 0.07 and 0.35 µm, that could be due to the decalcification of some C-S-H phases [70].

Within the zone sheltered from drying, the curve obtained at 63 ± 5 mm exhibits the densest gel and capillary porosities. This means that the core of the material, which already has the lowest porosity (Fig. 8-a), presents the densest microstructure. In fact, the zone contains the highest amount of water available in the pores, which leads to the highest hydration level, and thus to the highest amount of hydrates. This leads to the lowest porosity and the densest microstructure.

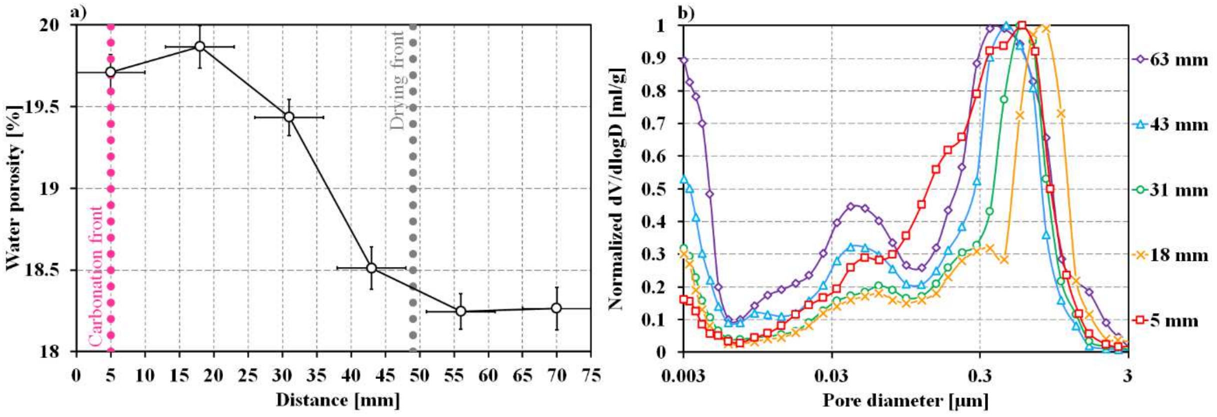

Fig. 8. Profiles of: **(a)** water porosity and **(b)** pore size distribution by MIP obtained after 6-month exposure.

3.2.6. Carbonation potential profile

The profiles after 6-month exposure show that hydric, hydration and microstructural properties are not uniform along the material (Figs. 5, 7 and 8). When approaching the exposed surface, due to the early drying, the material becomes less wet, less hydrated, less dense, and more porous. This causes a gradient of transfer properties between the exposed surface and the core of the material, which facilitates the exchanges with the surrounding environment near the surface. For instance, regarding the progress of carbonation front (Fig. 6), low water saturation degree (Fig. 5-b), combined with high porosity and coarse microstructure (Fig. 8), lead to an easier diffusion of CO_2 gas into the surface layer. Moreover, low hydration level (Fig. 7), combined with optimal hydric conditions (Fig. 5), facilitate chemical reactions between the dissolved CO_2 and the carbonatable products. The main properties that should be considered to roughly assess the progress of carbonation depth, in terms of *pH* drop, are at least: porosity, water saturation degree and Portlandite content [28,63,71,73]. These three parameters can be combined in a simplified parameter called "carbonation potential", obtained from simplification of a classical carbonation model [71], where the time-evolution of the carbonation depth is usually assessed by the empirical expression given in Eq. 11 [28,63,71–73]:

$$X_C = \alpha \sqrt{\frac{\varepsilon(1-S)}{CH}} \sqrt{t} \tag{11}$$

with: X_c [m] is the carbonation depth at time t [s], ε [-] is the water porosity (Eq. 10), S [-] is the water saturation degree (Eq. 7) and CH [-] is the Portlandite content (Eq. 9). The parameter α mainly depends on the diffusion coefficient of CO_2 in the air and concentration of CO_2 in the air. The simplified expression $(\varepsilon(1\text{–}S)/CH)^{1/2}$ is the carbonation potential which governs the carbonation kinetics [28]. The profile of carbonation potential after 6-month exposure is plotted in Fig. 9. As expected, the carbonation potential is not uniform along the material. There is a strong gradient between the exposed surface and the core of the material. The carbonation potential calculated at 5 ± 5 mm is about 5 times higher than that calculated within the core of the material. The risk of carbonation is then higher within the surface layer where the carbonation potential is the highest, i.e., where the conditions required for carbonation are optimal in terms of CO_2 availability, hydric conditions, and amount of carbonatable products. After that, the risk of carbonation is decreased with the decrease in potential carbonation. The main drawback of the simplified expression of carbonation potential is the fact that carbonation reactions do not occur when water saturation degree is too low. In fact, as carbonation occurs in the pore solution after dissolution of CO_2 [19,63,71–78], a very low degree of saturation due to a small amount of water available in the pores (Section 3.2.2), strongly limits this dissolution, which prevents carbonation [73–78]. This means that CO_2 diffuses freely within the pore network without however reacting with the cementitious matrix [19]. Therefore, a very high value of carbonation potential, due to a very low water saturation degree, does not necessarily imply a high risk of carbonation. However, the simplified expression shows that considering properties only within the core of the material, sheltered from drying, significantly underestimates the risk of carbonation due to the strong carbonation potential gradient between the exposed surface and the core of the material. This finding could be extended to other transfer properties (such as gas diffusivity and permeability, water absorption and sorptivity, and chloride permeability, etc.), especially to properties within the cover-zone of reinforced concrete which govern the transfer of aggressive agents, and thus control the risk of corrosion.

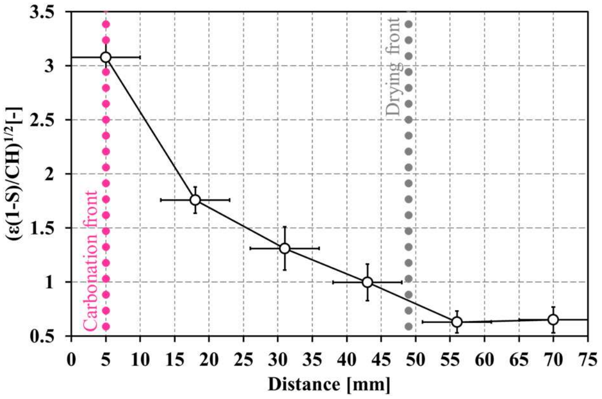

Fig. 9. Profile of carbonation potential obtained after 6-month exposure.

4. Conclusions

An experimental study of interactions between hydration and early drying was carried out on a mortar designed with a volume of GGBFS as high as the volume of OPC. The mortar was subjected, 1 day after casting, to 6-month unidirectional drying in natural surrounding conditions. The objective was to highlight and quantify the effects of early drying on hydration and microstructural properties of the material, especially those governing the carbonation kinetics. The main conclusions on the profiles after 6-month exposure are the following:

- Profiles of relative humidity, water content, water saturation degree, Portlandite content, and water porosity exhibit a drying depth of about 49 mm along which the shape of the profiles is strongly affected by early drying.
- Along the drying depth, the increase in water consumption by hydration, and mainly by drying, causes a decrease in the amount of water available in the pores. This induces a decrease in relative humidity (– 25 %), water content (– 82.23 %), water saturation degree (– 72.05 %), and Portlandite content expressing the hydration level (– 41.43 %). The

decrease in hydration level causes an increase in porosity (+ 8.03 %), and a coarsening of the microstructure, thus a lowering in the quality of the transfer properties. This facilitates the exchanges with the surrounding environment near the surface and lowers the resistance against the penetration of aggressive agents.

- Beyond the drying front, as the core of the material is sheltered from drying, it contains the highest amount of water available in the pores. This leads to the highest hydration level, which leads to the highest amount of hydrates, and thus to the lowest porosity and the densest microstructure and transfer properties.
- Water porosity (ε), water saturation degree (S) and Portlandite content (CH) were combined in a simplified parameter, called "carbonation potential" $(\varepsilon(1-S)/CH)^{1/2}$, build from the simplification of a classical carbonation model. The carbonation potential exhibits a strong gradient between the exposed surface and the core of the material. The value calculated near the exposed surface is about 5 times higher than that calculated within the core of the material.
- The risk of carbonation is higher within the surface layer where the carbonation potential is the highest. After that, the risk of carbonation is decreased with the decrease in potential carbonation.
- The carbonation potential shows that considering properties only within the core of the material, sheltered from drying, significantly underestimates the risk of carbonation due to the strong carbonation potential gradient between the exposed surface and the core of the material.

Based on these results, the effects of early drying on properties of concrete with low clinker content should not be overlooked. When early drying is unavoidable, which is often the case on construction site for practical and economic reasons, it would be better to characterize the concrete at different distances from the exposed surface, especially when the properties studied govern the transfer of aggressive agents.

The study of effects of early drying should be extended to other properties, such as gas diffusivity and permeability, water absorption and sorptivity, and chloride permeability, etc. The results should be implemented in models for predicting service life of reinforced concrete structures to better quantify the effect of spatial variability of properties, due to early drying, on service life.

References

[1] C. Carreño-Gallardo, A. Tejeda-Ochoa, O.I. Perez-Ordonez, J.E. Ledezma-Sillas, D. Lardizabal-Gutierrez, C. Prieto-Gomez, J.A. Valenzuela-Grado, F.C. Robles Hernandez, J.M. Herrera-Ramirez, In the CO_2 emission remediation by means of alternative geopolymers as substitutes for cements, J. Environ. Chem. Eng. 6 (2018) 4878–4884, https://doi.org/10.1016/j.jece.2018.07.033.

[2] A.R. Berenguer, A.P.B. Capraro, M.H. Farias de Medeiros, A.M.P. Carneiro, R.A. De Oliveira, Sugar cane bagasse ash as a partial substitute of Portland cement: Effect on mechanical properties and emission of carbon dioxide, J. Environ. Chem. Eng. 8 (2020) 103655, https://doi.org/10.1016/j.jece.2020.103655.

[3] F.N. Costa, D.V. Ribeiro, Reduction in CO_2 emissions during production of cement, with partial replacement of traditional raw materials by civil construction waste (CCW), J. Clean. Prod. 276 (2020) 123302, https://doi.org/10.1016/j.jclepro.2020.123302.

[4] G. Moumin, M. Ryssel, L. Zhao, P. Markewitz, C. Sattler, M. Robinius, D. Stolten, CO_2 emission reduction in the cement industry by using a solar calciner, Renew. Energy 145 (2020) 1578–1596, https://doi.org/10.1016/j.renene.2019.07.045.

[5] C. Ren, W. Wang, Y. Yao, S. Wu, Qamar, X. Yao, Complementary use of industrial solid

wastes to produce green materials and their role in CO_2 reduction, J. Clean. Prod. 252 (2020) 119840, https://doi.org/10.1016/j.jclepro.2019.119840.

[6] M.A. Sanjuán, C. Argiz, P. Mora, A. Zaragoza, Carbon Dioxide Uptake in the Roadmap 2050 of the Spanish Cement Industry, Energies 13 (2020) 3452, https://doi.org/10.3390/en13133452.

[7] Council of the European Union, UE. 2020. Long-term low greenhouse gas emission development strategy of the European Union and its Member States – Submission to the UNFCCC on behalf of the European Union and its Member States. No. prev. doc.: 6348/20. CLIMA 54. ENV 158. ONU 12. Brussels, Belgium, 5th of March 2020, https://data.consilium.europa.eu/doc/document/ST-6612-2020-INIT/en/pdf.

[8] S.M.R.A. Esfahani, S.A. Zareei, M. Madhkhan, F. Ameri, J. Rashidiani, R.A. Taheri, Mechanical and gamma-ray shielding properties and environmental benefits of concrete incorporating GGBFS and copper slag, J. Build. Eng. 33 (2021) 101615, https://doi.org/10.1016/j.jobe.2020.101615.

[9] S.A. Miller, A. Horvath, P.J.M. Monteiro, Readily implementable techniques can cut annual CO_2 emissions from the production of concrete by over 20%, Environ. Res. Lett. 11 (2016) 074029, https://doi.org/10.1088/1748-9326/11/7/074029.

[10] J.G.J. Olivier, G. Janssens-Maenhout, M. Muntean, J.A.H.W. Peters, Trends in global CO_2 emissions: 2016 report, PBL Netherlands Environmental Assessment Agency, European Commission, Joint Research Centre, 2016, https://www.pbl.nl/en/publications/trends-in-global-co2-emissions-2016-report.

[11] T.H. Lim, B.L. Ellis, S.J. Skerlos, Mitigating CO_2 emissions of concrete manufacturing through CO_2-enabled binder reduction, Environ. Res. Lett. 14 (2019) 114014, https://doi.org/10.1088/1748-9326/ab466e.

[12] E. Gartner, H. Hirao, A review of alternative approaches to the reduction of CO_2

emissions associated with the manufacture of the binder phase in concrete, Cem. Concr. Res. 78 (2015) 126–142, http://dx.doi.org/10.1016/j.cemconres.2015.04.012.

[13] M. Elchalakani, H. Basarir, A. Karrech, Green concrete with high-volume fly ash and slag with recycled aggregate and recycled water to build future sustainable cities, J. Mater. Civ. Eng. 29 (2) (2017), https://doi.org/10.1061/(asce)mt.1943-5533.0001748.

[14] J.C. Chern, Y.W. Chan, Deformations of concrete made with blast-furnace slag cement and ordinary Portland cement, ACI Mater. J. 86 (1989) 372–382, https://doi.org/10.14359/2151.

[15] G.J. Osborne, Durability of Portland blast-furnace slag cement concrete, Cem. Concr. Compos. 21 (1999) 11–21, https://doi.org/10.1016/S0958-9465(98)00032-8.

[16] K.M. Lee, H.K. Lee, S.H. Lee, G.Y. Kim, Autogenous shrinkage of concrete containing granulated blast-furnace slag, Cem. Concr. Res. 36 (2006) 1279–1285, https://doi.org/10.1016/j.cemconres.2006.01.005.

[17] K. Bourbatache, O. Millet, A. Aït-Mokhtar, Ionic transfer in charged porous media. Periodic homogenization and parametric study on 2D microstructures, Int. J. Heat Mass Transfer 55 (2012) 5979–5991, https://doi.org/10.1016/j.ijheatmasstransfer.2012.06.008.

[18] A. Younsi, Ph. Turcry, A. Aït-Mokhtar, S. Staquet, Accelerated carbonation of concrete with high content of mineral additions: effect of interactions between hydration and drying, Cem. Concr. Res. 43 (2013) 25–33, https://doi.org/10.1016/j.cemconres.2012.10.008.

[19] Ph. Turcry, L. Oskri-Neflia, A. Younsi, A. Aït-Mokhtar, Analysis of an accelerated carbonation test with severe preconditioning, Cem. Concr. Res. 57 (2014) 70–78, https://doi.org/10.1016/j.cemconres.2014.01.003.

[20] N. Issaadi, A. Nouviaire, R. Belarbi, A. Aït-Mokhtar, Moisture characterization of cementitious material properties: Assessment of water vapor sorption isotherm and permeability variation with ages, Constr. Build. Mater. 83 (2015) 237–247,

https://doi.org/10.1016/j.conbuildmat.2015.03.030.

[21] D.M. Roy, G.M. Idorn, Hydration, structure, and properties of blast furnace slag cements, mortars, and concrete, J. Am. Concr.e Inst. 79 (1982) 444–457, https://doi.org/10.14359/10919.

[22] J.J. Escalante, L.Y. Gomez, K.K. Johal, G. Mendoza, H. Mancha, J. Mendez, Reactivity of blast-furnace slag in Portland cement blends hydrated under different conditions, Cem. Concr. Res. 31 (2001) 1403–1409, https://doi.org/10.1016/S0008-8846(01)00587-7.

[23] T.C. Powers, A discussion of cement hydration in relation to the curing of concrete, Proc. Highw. Res. Board 27 (1947) 178–188.

[24] W.H. Price, Factors influencing concrete strength, Proc. Am. Concr. Inst. 47 (1951) 417–432.

[25] R.G. Patel, D.C. Killoh, L.J. Parrott, W.A. Gutteridge, Influence of curing at different relative humidities upon compound reactions and porosity in Portland cement paste, Mater. Struct. 21 (1988) 192–197, https://doi.org/10.1007/BF02473055.

[26] T. Powers, L. Copeland, J. Hayes, H. Mann, Permeability of Portland cement paste, J. Proc. 51 (1954) 285–298.

[27] J. Parrot, Novel methods of processing cement gel to examine and control microstructure and properties, R. Soc. 310 (1983) 155–166, https://doi.org/10.1098/rsta.1983.0074.

[28] A. Younsi, P. Turcry, A. Aït-Mokhtar, S. Staquet, Numerical study of the influence of drying on properties governing the carbonation mechanism of concretes with low clinker content, Eur. J. Environ. Civ. Eng. 23 (2019) 172–192, https://doi.org/10.1080/19648189.2016.1271364.

[29] O.M. Jensen, Thermodynamic limitation of self-desiccation, Cem. Concr. Res. 25 (1995) 157–164, https://doi.org/10.1016/0008-8846(94)00123-G.

[30] O.M. Jensen, P.F. Hansen, E.E. Lachowski, F.P. Glasser, Clinker mineral hydration at

reduced relative humidities, Cem. Concr. Res. 29 (1999) 1505–1512, https://doi.org/10.1016/S0008-8846(99)00132-5.

[31] K.A. Snyder, D.P. Bentz, Suspended hydration and loss of freezable water in cement pastes exposed to 90% relative humidity, Cem. Concr. Res. 34 (2004) 2045–2056, https://doi.org/10.1016/j.cemconres.2004.03.007.

[32] R.J. Flatt, G.W. Scherer, J.W. Bullard, Why alite stops hydrating below 80% relative humidity, Cem. Concr. Res. 41 (2011) 987–992, https://doi.org/10.1016/j.cemconres.2011.06.001.

[33] M. Wyrzykowski, P. Lura, Effect of relative humidity decrease due to selfdesiccation on the hydration kinetics of cement, Cem. Concr. Res. 85 (2016) 75–81, https://doi.org/10.1016/j.cemconres.2016.04.003.

[34] A. Younsi, A. Bordy, S. Aggoun, B. Fiorio, Hydration-drying interactions in OPC pastes blended with recycled OPC paste fine powder: critical curing relative humidity hampering hydration, Constr. Build. Mater. 90 (2018) 403–413, https://doi.org/10.1016/j.conbuildmat.2018.09.132.

[35] C.M. Neubauer, H.M. Jennings, E.J. Garboczi, Mapping drying shrinkage deformation in cement based materials, Cem. Concr. Res. 27 (1997) 1603–1612, https://doi.org/10.1016/S0008-8846(97)00217-2.

[36] H.M. Jennings, J.J. Thomas, J.S. Gevrenov, G. Constantinides, F.-J. Ulm, A multi-technique investigation of the nanoporosity of cement paste, Cem. Concr. Res. 37 (2007) 329–336, https://doi.org/10.1016/j.cemconres.2006.03.021.

[37] R. Patel, L. Parrott, J. Martin, D. Killoh, Gradients of microstructure and diffusion properties in cement paste caused by drying, Cem. Concr. Res. 15 (1985) 343–356, https://doi.org/10.1016/0008-8846(85)90046-8.

[38] L.J. Parrott, Variations of water absorption rate and porosity with depth from an exposed

concrete surface – effects of exposure conditions and cement type, Cem. Concr. Res. 22 (1992) 1077–1088, https://doi.org/10.1016/0008-8846(92)90038-W.

[39] Y. Ballim, Curing and the durability of OPC, fly ash and blast-furnace slag concretes, Mater. Struct. 26 (1993) 238–244, https://doi.org/10.1007/BF02472617.

[40] M.A. Sanjuán, A. Piñeiro, O. Rodríguez, Ground granulated blast furnace slag efficiency coefficient (k value) in concrete. Applications and limits, Mater. Constr. 61 (2011) 303–313, http://dx.doi.org/10.3989/mc.2011.60410.

[41] M. A. Sanjuan, E. Estevez, C. Argiz, D. del Barrio, Effect of curing time on granulated blast-furnace slag cement mortars carbonation, Cem. Concr. Compos. 90 (2018) 257–265, https://doi.org/10.1016/j.cemconcomp.2018.04.006.

[42] E. Gruyaert, P.V.d. Heede, N.D. Belie, Carbonation of slag concrete: effect of the cement replacement level and curing on the carbonation coefficient–effect of carbonation on the pore structure, Cem. Concr. Compos. 35 (2013) 39–48, https://doi.org/10.1016/j.cemconcomp.2012.08.024.

[43] A. Neville, Chloride attack of reinforced concrete: an overview, Mater. Struct. 28 (1995) 63–70, https://doi.org/10.1007/BF02473172.

[44] M.F. Montemor, A.M.P. Simoes, M.G.S. Ferreira, Chloride-induced corrosion on reinforcing steel: from the fundamentals to the monitoring techniques, Cem. Concr. Compos. 25 (2003) 491–502, https://doi.org/10.1016/S0958-9465(02)00089-6.

[45] O. Poupard, A. Aït-Mokhtar, P. Dumargue, Impedance spectroscopy in reinforced concrete: experimental procedure for monitoring steel corrosion – part I: development of the experimental device, J. Mater. Sci. 38 (2003) 2845–2850, https://doi.org/10.1023/A:1024428317968.

[46] O. Poupard, A. Aït-Mokhtar, P. Dumargue, Impedance spectroscopy in reinforced concrete: Experimental procedure for monitoring steel corrosion – Part II: Polarization effect.

J. Mater. Sci. 38 (2003) 3521–3526, https://doi.org/10.1023/A:1025600624991.

[47] O. Poupard, A. Aït-Mokhtar, P. Dumargue, Corrosion by chlorides in reinforced concrete: Determination of chloride concentration threshold by impedance spectroscopy, Cem. Concr. Res. 34 (2004) 991–1000, https://doi.org/10.1016/j.cemconres.2003.11.009.

[48] R. M. Ghantous, S. Poyet, V. L'Hostis, N.-C. Tran, R. François, Effect of crack openings on carbonation-induced corrosion, Cem. Concr. Res. 95 (2017) 257–269, https://doi.org/10.1016/j.cemconres.2017.02.014.

[49] A.E.M. Abd Elmoaty, Four-years carbonation and chloride induced steel corrosion of sulfate-contaminated aggregates concrete, Constr. Build. Mater. 163 (2018) 539–556, https://doi.org/10.1016/j.conbuildmat.2017.12.128.

[50] P.K. Mehta, Concrete. Structure, properties and materials 1986.

[51] I.G. Richardson, G.W. Groves, Microstructure and microanalysis of hardened cement pastes involving ground granulated blast-furnace slag, J. Mater. Sci. 27 (1992) 6204–6212, https://doi.org/10.1007/BF01133772.

[52] W. Chen, H.J. Brouwers, The hydration of slag, part 2: reaction models for blended cement, J. Mater. Sci. 42 (2007) 444–464, https://doi.org/10.1007/s10853-006-0874-1.

[53] EN 197-1 Standard, Cement – Part 1: Composition, specifications and conformity criteria for common cements, 2011.

[54] EN 15167-1 Standard, Ground granulated blast furnace slag for use in concrete, mortar and grout – Part 1: Definitions, specifications and conformity criteria, 2006.

[55] EN 13139 Standard, Aggregates for mortar, 2003.

[56] A. Bordy, A. Younsi, S. Aggoun, B. Fiorio, Cement substitution by a recycled cement paste fine: role of the residual anhydrous clinker, Constr. Build. Mater. 132 (2017) 1–8, https://doi.org/10.1016/j.conbuildmat.2016.11.080.

[57] B. Persson, Self-desiccation and its importance in concrete technology, Mater. Struct. 30

(1997) 293–305, https://doi.org/10.1007/BF02486354.

[58] EN 206+A1 Standard, Concrete – Specification, performance, production and conformity, 2016.

[59] EN 196-1 Standard, Methods of testing cement – Part 1: Determination of strength, 2016.

[60] A. Trabelsi , A. Hamami , R. Belarbi , P. Turcry, A. Aït-Mokhtar, Assessment of the variability of moisture transfer properties of High Performance Concrete from a multi-stage drying experiment, Eur. J. Environ. Civ. Eng. 16 (2012) 352–361, https://doi.org/10.1080/19648189.2012.667713.

[61] A. Trabelsi, P. Turcry, R. Belarbi, A. Aït-Mokhtar, Water vapour desorption variability of in situ concrete and effects on drying simulations, Mag. Concr. Res. 63 (2011) 333–342, https://doi.org/10.1680/macr.9.00161.

[62] NF P18-459 Standard, Concrete – Testing hardened concrete – Testing porosity and density (in French), 2010.

[63] M. Thiery, G. Villain, P. Dangla, G. Platret, Investigation of the carbonation front shape on cementitious materials: effects of the chemical kinetics, Cem. Concr. Res. 37 (2007) 1047–1058, https://doi.org/10.1016/j.cemconres.2007.04.002.

[64] EN 12390-12 Standard, Testing hardened concrete – Part 12: Determination of the carbonation resistance of concrete – Accelerated carbonation method, 2020.

[65] ISO 15901-1 Standard, Evaluation of pore size distribution and porosity of solid materials by mercury porosimetry and gas adsorption – Part 1: Mercury porosimetry, 2016.

[66] J.-K. Kim, C.-S. Lee, Moisture diffusion of concrete considering self-desiccation at early ages, Cem. Concr. Res. 29 (1999) 1921–1927, https://doi.org/10.1016/S0008-8846(99)00192-1.

[67] O. Omikrine Metalssi, A. Aït-Mokhtar, P. Turcry, A proposed modelling of coupling carbonation-porosity-moisture transfer in concrete based on mass balance equilibrium, Constr.

Build. Mater. 230 (2020) 116997, https://doi.org/10.1016/j.conbuildmat.2019.116997.

[68] P.C. Kreijger, The skin of concrete composition and properties, Mat. Constr. 17 (1984) 275–283, https://doi.org/10.1007/BF02479083.

[69] H.M. Jennings, A. Kumar, G. Sant, Quantitative discrimination of the nano-pore-structure of cement paste during drying: new insights from water sorption isotherms Cem. Concr. Res. 76 (2015) 26–36, https://doi.org/10.1016/j.cemconres.2015.05.006.

[70] G.W. Groves, A. Brough, I.G. Richardson, C.M. Dobson, Progressive changes in the structure of hardened C_3S cement pastes due to carbonation, J. Am. Ceram. Soc. 74 (1991) 2891–2896, https://doi.org/10.1111/j.1151-2916.1991.tb06859.x.

[71] V.G. Papadakis, C.G. Vayenas, M.N. Fardis, A reaction engineering approach to the problem of concrete carbonation, J. Am. Inst. Chem. Eng. 1 (1989) 110–122, https://doi.org/10.1002/aic.690351008.

[72] R. Millington, Gas diffusion in porous media, Science 130 (1959) 100–102, https://doi.org/10.1126/science.130.3367.100-a.

[73] V.G. Papadakis, C.G. Vayenas, M.N. Fardis, Fundamental modeling and experimental investigation of concrete carbonation, ACI Mater. J. 88 (1991) 363–373, https://doi.org/10.14359/1863.

[74] V.A. Juvekar, M.M. Sharma, Absorption of CO_2 in a suspension of lime, Chem. Eng. Sci. 28 (1973) 825–837, https://doi.org/10.1016/0009-2509(77)80017-1.

[75] G.J. Verbeck, Carbonation of hydrated Portland cement, ASTM Spec. Tech. Publ. 205 (1958) 17–36, https://doi.org/10.1520/STP39460S.

[76] L. De Ceukelaire, D. Van Nieuwenburg, Accelerated carbonation of a blast furnace cement concrete, Cem. Concr. Res. 23 (1993) 442–452, https://doi.org/10.1016/0008-8846(93)90109-M.

[77] K. Van Balen, D. Van Gemert, Modelling lime mortar carbonation, Mater. Struct. 27

(1994) 393–398, https://doi.org/10.1007/BF02473442.

[78] S.K. Roy, K.B. Poh, D.o. Northwood, Durability of concrete-accelerated carbonation and weathering studies, Build. Environ. 34 (1999) 597–606, https://doi.org/10.1016/S0360-1323(98)00042-0.